International Journal of Nanomedicine

Dovepress
open access to scientific and medical research

Open Access Full Text Article

ORIGINAL RESEARCH

Targeted and pH-facilitated theranostic of orthotopic gastric cancer via phase-transformation doxorubicin-encapsulated nanoparticles enhanced by low-intensity focused ultrasound (LIFU) with reduced side effect

This article was published in the following Dove Press journal:
International Journal of Nanomedicine

Zhangluxi Liu[1]
Haitao Ran[2]
Zhigang Wang[2]
Shiji Zhou[1]
Yaxu Wang[1]

[1]Department of Gastrointestinal Surgery, Second Affiliated Hospital of Chongqing Medical University, Chongqing 400010, People's Republic of China; [2]Institute of Ultrasound Imaging of Chongqing Medical University, Chongqing 400010, People's Republic of China

Purpose: Focused ultrasound-mediated chemotherapy, as a non-invasive therapeutic modality, has been extensively explored in combating deep tumors for predominant penetration performance. However, the generally used high-intensity focused ultrasound (HIFU) inevitably jeopardizes normal tissue around the lesion for hyperthermal energy. To overcome this crucial issue, low-intensity focused ultrasound (LIFU) was introduced to fulfill precisely controlled imaging and therapy in lieu of HIFU. The objective of this study was to develop a facile and versatile nanoplatform (DPP-R) in response to LIFU and provide targeted drug delivery concurrently.

Methods: Multifunctional DPP-R was fabricated by double emulsion method and carbodiimide method. Physicochemical properties of DPP-R were detected respectively and the biocompatibility and bio-safety were evaluated by CCK-8 assay, blood analysis, and histologic section. The targeted ability, imaging function, and anti-tumor effect were demonstrated in vitro and vivo.

Results: The synthetic DPP-R showed an average particle size at 367 nm, stable physical-chemical properties in different media, and high bio-compatibility and bio-safety. DPP-R was demonstrated to accumulate at the tumor site by active receptor/ligand reaction and passive EPR effect with intravenous administration. Stimulated by LIFU at the tumor site, phase-transformable PFH was vaporized in the core of the integration offering contrast-enhanced ultrasound imaging. The stimuli led to encapsulated DOX's initial burst release and subsequent sustained release for anti-tumor therapy which was verified to be more effective and have less adverse effects than free DOX.

Conclusion: DPP-R combined with LIFU provides a novel theranostic modality for GC treatment with potent therapeutic effect, including prominent performance of targeting, ultrasound imaging, and accurate drug release.

Keywords: low-intensity focused ultrasound, nanoparticles, phase-transition, gastric cancer, targeted anti-cancer therapy

Correspondence: Yaxu Wang; Shiji Zhou
Department of Gastrointestinal Surgery, Second Affiliated Hospital of Chongqing Medical University, Chongqing 400010, People's Republic of China
Email wangyaxuhospital@163.com; zhoushiji@hospital.cqmu.edu.cn

Introduction

Gastric cancer (GC) is a common malignancy and the second leading cause of cancer-related mortality worldwide.[1] Most newly confirmed patients are at an advanced stage due to lack of specific symptoms, positive signs or active screening programs at the

submit your manuscript | www.dovepress.com
DovePress
http://doi.org/10.2147/IJN.S212888

early stage. As a result, the therapy relies on radiotherapy, chemotherapy, and other adjuvant therapy to a great extent, however, it provides no significant improvement in the long-term survival.[2] Therefore, researchers are prompted to develop a novel and credible approach for GC diagnosis and therapy to improve the theranostic status of sufferers. Based on the dominant trend of theranostic integration in recent years, acoustic-responsive polymer probes, due to their non-invasion, non-radiation, precision and specificity characteristics, have become a hot topic.[3,4]

Acoustic-responsive polymer probes, endowed with the ability to be a targeting ultrasound (US) contrast agent (UCA), are the core and cornerstone of US molecular imaging and are often designed as a microbubbles (MBs) or nanoparticles (NPs) model, for instance liposome, inorganic mesoporous, organic polymer, etc. Compared with MBs, NPs exhibit smaller particle size, stronger penetrability, longer pharmacokinetics circulation, preferable stability, and easier surface modification capability.[5] Nevertheless, the poor acoustic responsiveness of NPs induced by the substantially decreased particle size cannot be ignored in the meantime.[5] The employment of phase-transformable liquid fluorocarbon solves this crucial problem by externally stimulating the liquid-gas phase-transition within NPs.[6,7] As a trigger of acoustic droplet vaporization (ADV), low-intensity focused ultrasound (LIFU) shares plenty of particular characteristics with high-intensity focused ultrasound (HIFU), such as high spatial resolution and focused stimulation.[8] However, HIFU will indistinguishably ablate the surrounding and intervening normal tissue through thermal effect,[8] which is nonexistent in LIFU. In addition, compared with another popular trigger of vaporization-near-infrared (NIR) light, LIFU is capable of penetrating more deeply to act on internal deep organs or tissue.[9] A growing number of studies have demonstrated the competitive advantages of LIFU in tumor imaging and therapy, such as non-thermal performance, focused US power, deep penetration, cavitation effect, and sonodynamic motivation.[10,11]

PLGA is one of the most promising polymeric materials to assemble phase-transformable NPs complex owing to its excellent bio-compatibility and biodegradability.[12] In addition, the porous and elastic structure of PLGA NPs gives it a unique drug loading, delivering, and releasing benefit.[13,14] Recent studies have revealed that LIFU sonication can accurately steer drug release, meanwhile, locally facilitate the diffusion and penetration of drugs.[15,16] Among the chemotherapeutics regularly used in clinical GC treatment, DNA-binding medicine, doxorubicin (DOX) has always been widely used due to its excellent anti-proliferation and apoptosis-promoting effect.[17] However, with the defect of non-specific distribution in organs and the high blood concentration needed to fulfill the therapeutic dose, DOX will indiscriminately attack proliferating tumor and normal tissue cells, sequentially leading to severe systemic toxicity, such as myelosuppression and cardiotoxicity, thus greatly limiting its therapeutic potential.[18] Fortunately, LIFU-mediated drug administration is able to control the time point and location of drug release which may remarkably decrease the systemic adverse effect by localizing the bio-toxicity.[19] To achieve the active targeting ability, accurate site-specific drug delivery and accumulation effect, RGD peptide was introduced into the nanocomposite which is the specific ligand of the over-expressed integrin $\alpha v\beta_3$ on GC cells.[20,21]

Based on all the grounds mentioned previously, this study synthesized a novel multifunctional core-shell structure nanocomposite DOX/PFH@PLGA-RGD(DPP-R) with LIFU-mediated to optimize the diagnosis and therapy of GC. In the resultant nanoscale matrix, PLGA offered its appealing loading ability to be the shell which encapsulated the chemotherapy drug DOX and acoustic-responsive material perfluorohexane (PFH). RGD was covalently connected to the surface of DOX/PFH-loaded PLGA NPs via carbodiimide method. For reliable results, orthotopic tumor model was adopted to detect the feasibility of DPP-R combined with LIFU. The advantageous features of non-invasiveness, ligand/receptor-mediated targeting, LIFU-triggered phase-transformation, accurate drug release, and LIFU-induced cavitation effect endowed DPP-R with favorable ability to be an unprecedented integrated system of diagnosis and therapy utilized in GC.

Experimental section

Materials

PLGA-COOH (molecular weight 12,000 Da) was obtained from Daigang Biomaterial Co. (Jinan, People's Republic of China). DOX was purchased from MACKLIN Biochemical Technology CO (Shanghai, People's Republic of China). RGD (RGDfk-FITC, c(RGDfk)) was purchased from GL Biochem Ltd (Shanghai, People's Republic of China). PFH, polyvinyl alcohol (PVA, molecular weight 26 kDa), 2-(N-morpholino) ethanesulfonic acid (MES monohydrate), N-(3-dimethyl-aminopropyl)-N'-ethylcarbodiimide hydrochloride (EDC), 1,1′-dioctadecyl-3,3,3′,3′-tetramethylindo-tricarbocyanine iodide (DiR), 4′,6-diamidino-2-phenylindole (DAPI), and N-hydroxysuccinimide (NHS) were purchased from Sigma-Aldrich

Co. (St Louis, MO, USA). High glucose dulbecco's modified eagle medium (DMEM) and fetal bovine serum (FBS) were purchased from Gibco Co. (Carlsbad, CA, USA). Cell Counting Kit-8 (CCK-8) was purchased from Dojindo Molecular Technology (Shanghai, People's Republic of China). Trichloromethane and isopropanol were purchased from Chongqing Chuandong Chemicals (Chongqing, People's Republic of China). All other reagents used in this work were of analytical grade and were used as received.

Synthesis of DPP and DPP-R

DPP-R was synthesized via a double emulsion method. First, 200 μL PFH was added into 2 mL trichloromethane ($CHCl_3$). The mixture was emulsified for 2 min (3 s on, 5 s off) at 25% intensity using an ultrasonic probe (VCX-130; SONICS & MATERALS Inc; USA) in ice bath through the entire process and simultaneously 200 μL DOX aqueous solution was added dropwise. Subsequently, 5 mL 4% PVA aqueous solution was added into the pre-emulsion followed by the second sonication for 5 min (3 s on, 5 s off) at 25% intensity. Next, 10 mL 2% isopropanol was added into the nanodroplets and then stabilized with the use of magnetic stirring apparatus (HJ-1, Ronghua, People's Republic of China) for 3 h to volatilize the organic solvent. Finally, the non-targeting DOX/PFH@PLGA(DPP) was obtained after centrifugation (centrifuge, 5804R; Eppendorf, Hamburg, Germany) at 10,000 rpm for 8 min three times.

Afterward, DPP was covalently modified by the RGD peptide on the surface of the shell to get DPP-R by carbodiimide method. First, DPP was resuspended in MES buffer (0.1 M, pH=6.0), activated by activator at the molar ratio PLGA-COOH: EDC: NHS=1:10:30 for 1 h with mild shaking and centrifuged three times to clear redundant activator. Next the activated nanodroplets were resuspended in another MES buffer (0.1 M, pH=8.0), co-incubated with RGD peptide at the molar ratio PLGA-COOH: RGD=1:1 for 1.5 h, and also centrifuged three times to eliminate the free peptide. Pure NPs such as PFH@PLGA-RGD(PP-R) and PFH@PLGA(PP) were prepared on the basis of previously mentioned procedure except the encapsulation of DOX or PFH. All the NPs were stored at 4°C.

Characterization of DPP-R

The morphology and nanostructure of DPP-R was observed using an optical microscope (CKX41; Olympus Corporation, Tokyo, Japan) and transmission electron microscope (TEM) (H-7500; Hitachi Ltd., Tokyo, Japan). The connection of RGD was observed by a confocal laser scanning microscope (CLSM; Nikon A1, Nikon Corporation, Tokyo, Japan) and flow cytometry method (FCM; FACSVantage, BD, USA) was used to measure the binding efficiency. The particle size distribution and zeta potential were determined by a Laser Particle Size Analyzer System (Nano, ZS90, Malvern Instruments, Malvern, UK). The size change induced by drug loading and peptide connecting was also detected. In order to evaluate the stability of DPP-R, its particle size and PDI were measured for 7 days in three different media (PBS, FBS, and high glucose DMEM) at room temperature and at the same time its morphology was observed by scanning electron microscope (SCM; JSM-7800F; JEOL, Tokyo, Japan). The absorption spectrum of free DOX, PP, and DPP was detected by a UV-VIS-NIR spectrophotometer (UV2550, Shimadzu, Japan). The unentrapped DOX was analyzed by comparing the absorption spectrum of supernatant with standard curve, which was depicted based on the absorption spectra of different DOX concentrations. DOX entrapment efficiency and content were calculated by the following equation:[22]

$$\text{Entrapment efficiency}(\%)\ (\text{EE}) = (\text{Total DOX} - \text{Unentrapped DOX})\,/\text{Total DOX}$$

$$\text{Loading capacity}(\%)\ (\text{LC}) = (\text{Total DOX} - \text{Unentrapped DOX})/\text{Total NPs}$$

Cell culture and MGC-803 orthotopic tumor-bearing mice model

The human GC MGC-803 cell line was obtained from Chongqing Medical University (Chongqing, People's Republic of China), which was approved by the Animal Ethics Committee of Chongqing Medical University and cultured in DMEM with 10% FBS and 1% penicillin/streptomycin and grown in an incubator with 5% CO2 and proper humidity at 37°C.

All female nude mice (weight of 14–16 g and age of 4–6 w) were purchased from Animal Experiment Center of Chongqing Medical University. All the experiments on animals were performed in compliance with international practices for animal care and use, after being approved by the Animal Ethics Committee of Chongqing Medical University. First, to establish the GC xenograft, 4×10^6 MGC-803 cells were harvested in 100 μL of serum-free DMEM and subcutaneously injected into the flank of the nude mice. The xenograft tumor was resected during the logarithmic growth stage

and the viable tumor tissue was cut into small pieces of 1 mm^3 volume. The nude mice were anesthetized with 1% pentobarbital sodium in an aseptic environment, then their greater curvature of gastric wall was exposed and slightly injured using an injector. The little tumor mass was sutured to the damaged stomach wall. The nude mice were fasted for 12 hrs after surgery.

In vitro DOX release

To assess the release ability of the drug-carrying NPs, 4 samples of DOX loaded NPs were gathered into prepared dialysis bags respectively which allowed molecules under 7 kDa infiltrating to outside PBS (pH=7.4/5.5) solution and shaken at 140 rpm at a homothermal temperature 37°C. 2 mL dialysis solution was taken out from the whole system every other hour during the total 72 h, meanwhile another 2 mL fresh PBS was added back. Specifically, 2 samples in different pH conditions were exposed to LIFU (8 W, 5 min) (50% duty cycle, pulse wave mode and the following procedure kept consistent) at 6 h while the other 2 samples were left without LIFU triggering. The concentration of DOX at presupposed different time points was measured by UV-VIS-NIR spectrophotometer.

For further verification of LIFU-mediated drug release, two groups of MGC-803 cells were co-incubated with DPP for 6 h. Subsequently, one group was exposed to LIFU (8 W, 5 min) while another was left without LIFU irradiation. After being dyed with DAPI for 5 min and fixed with 4% paraformaldehyde for 15 min, CLSM images of MGC-803 in two groups were obtained.

Bio-compatibility and bio-safety studies

To evaluate the in vitro bio-safety of PP-R, PP, and LIFU, MGC-803 cells were seeded in 96-well plates (8×10^3 per well) for 24 h. Then PP-R and PP were respectively resuspended in DMEM at different concentrations (0.15, 0.30, 0.625, 1.25, 2.50, and 5.00 μg/mL) and added into each well replacing previous medium followed by another 24 h co-incubation. The toxicity of separate LIFU irradiation was detected without any NPs and each well was exposed to different powers of LIFU (3 W, 4 W, 5 W, 6 W, 7 W, 8 W) for 5 min. Cell viability was tested by CCK-8 assay.

As to the in vivo bio-safety and bio-compatibility evaluation, three groups (n=9 per group) of healthy nude mice (8 weeks, 20–23 g), which were randomly acquired, respectively had PP-R, PP, and saline intravenously injected with corresponding agent (5 mg/mL). The blood and serum samples of mice were collected after 1 day, 7 days, 14 days respectively (3 mice were sacrificed for each group at different time points) for routine blood and blood biochemistry examination. The major organs (heart, liver, spleen, lung, and kidney) of mice were sectioned for histopathologic analysis using hematoxylin and eosin (H&E) staining.

Targeting ability of DPP-R

To demonstrate the targeting ability of DPP-R in vitro, MGC-803 cells were seeded into specific culture dishes (1×10^5 cells) for CLSM. After 24 h to allow adhesion, targeting DPP-R and none-targeting DPP were dispersed in DMEM at the same concentration, then added into dishes respectively and co-incubated for another 3 h. All the cells were dyed with DAPI for 5 min, DiO for 10 min, fixed with 4% paraformaldehyde for 15 min, and gently washed with PBS times. Finally, the dishes were observed with the use of CLSM. The binding efficiency was measured by FCM.

For the bio-distribution of targeting DPP-R and non-targeting DPP, a living florescence imaging (FLI) system (IVIS Lumina Series III; PerkinElmer Inc., Waltham, MA, USA) was employed to manifest at different time points. Since the liver and spleen were anatomically adjacent to the stomach, subcutaneous tumor-bearing nude mice were used to avoid the interplay between tumors and organs. All the nude mice were divided in two groups (n=3 per group) as follows: targeting group and non-targeting group intravenously injected with 200 μL DiR-labeled DPP-R and DiR-labeled DPP respectively at the concentration of 5 mg/mL. The living fluorescence images were taken at 1 h, 6 h, 24 h post-injection. Afterward, the major organs (heart, liver, spleen, lung, kidney, and brain) and tumors were harvested for the ex vivo fluorescence imaging. The fluorescence intensity of ex-vivo tumors and organs were quantified to compare the targeting effect between DPP-R and DPP and evaluate the bio-distribution of NPs.

Phase-transition properties and imaging function of DPP-R

As for the ADV property in vitro, LIFU was used to stimulate the vaporization of NPs in an agarose gel phantom at 4 W, 6 W, and 8 W respectively. The B-mode and contrast-enhanced ultrasound (CEUS) image of NPs were captured from 3 min, 4 min, 5 min, and 6 min. In the meantime, the post-stimulated nanodroplets were observed

with an optical microscope to visualize the resultant phase-transition.

For the ADV property in vivo, orthotopic tumor-bearing nude mice were randomly divided into three groups (n=3 per group) as follows: DPP-R+LIFU, DPP+LIFU, and DPP-R. After being injected with corresponding agent (5 mg/mL) for 6 h, the mice received intragastric gavage with traditional contrast agent to emerge the whole stomach area and then exposed to LIFU on midsection with the parameter of 8W for 5 min. MyLab 90 (Esaote, Italy) was used to generate the B-mode and CEUS images and the mean grayscale values of the region of interest (ROI) in vitro and vivo were obtained with DFY software.

In vitro cytotoxicity and in vivo therapeutic effect

MGC-803 cells were seeded in 96-well plates (8×10^3 per well) in the same way as mentioned previously to conduct the cytotoxicity experiment in vitro. Groups were: free DOX, DPP-R+LIFU, DPP+LIFU, DPP-R. After 24 h to allow adherence, MGC-803 cells were treated with different agents and conditions according to their groups. All the concentrations of NPs were unified to a settled gradient: 0.625, 1.25, 2.5, 5, and 10 μg/mL (an equivalent concentration of DOX) and after 3 h co-incubation, LIFU was settled at the parameter of 8W for 5 min to apply to DPP-R+LIFU and DPP+LIFU groups. After another 24 h co-incubation, cell viability was tested with CCK-8 assay.

To evaluate the therapeutic effect of DPP-R, fifteen MGC-803 orthotopic tumor-bearing mice were divided in 5 groups randomly. Groups were: free DOX, DPP-R+LIFU, DPP+LIFU, DPP-R, and control (n=3 per group). Each group was intravenously injected with corresponding NPs (the equivalent dose of DOX was kept at 2 mg/Kg)[23] except control group which was treated with saline. 6 h after the administration, DPP-R+LIFU and DPP+LIFU groups were anesthetized with 1% pentobarbital sodium and exposed to LIFU at 8 W for 5 min. The weight of all the mice were monitored after daily treatment which was conducted every three days. When the therapy procedure had been completed, tumors were excised for weighing and tumor inhibition rate (TIR) was calculated after the treatment strategy was repeated five times using the equation $TIR=(W_{control}-W_{treatment}/W_{control})\times100\%$. In the meantime, the major organs (heart, liver, spleen, lung, and kidney) were collected for H&E staining and the tumor tissue was sectioned for H&E and TdT-mediated dUTP Nick-End Labeling (TUNEL) staining to analyze the histopathologic characteristics and apoptosis of tumor cells post-therapy. Furthermore, blood samples of each mouse were collected for routine blood and myocardial enzyme examination to assess the adverse effect of DOX.

Statistical analysis

All experimental data were presented as mean ± standard deviation and disposed with SPSS 22.0 software. One-way ANOVA and Student's *t*-test were performed to determine the statistical significance among multiple groups and between two groups. *P*-values <0.05 suggested significant difference (*$p<0.05$).

Results and discussion

Design, fabrication and characterization of DPP-R

The novel bio-compatible multifunctional NPs DPP-R were elaborately engineered to be a nanoscale hollow sphere with the features of phase-transition for LIFU-synergistic imaging and accurate targeting chemotherapy in this study (Figure 1). To be specific, PLGA was selected to be the shell due to its excellent capability as a carrier with reliable stability, facile surface modification, stimuli responsiveness, and verified bio-safety.[24,25] The core was constituted with DOX and PFH by double emulsion method. According to reports, enormous potential of PFH has been exploited in US molecular imaging because of the phase-transition ability. Guo et al has utilized the desirable boiling temperature of PFH and researched the optical droplet vaporization (ODV) effect for cell permeability and facilitating drug delivery, which is actually the result of thermal effect induced by photothermal conversion.[26] Comparatively relevant research of ADV effect is rarely conducted. The power of mechanical wave generated by LIFU was capable of triggering liquid-to-gas transition of PFH, meanwhile enhancing the cavitation effect of vaporization.[27] In this study, the ADV effect of LIFU to PFH was assessed in vitro and vivo together with another appealing function: accurate drug release. An additional targeting ability endowed by RGD contributed to enhancing the in-site accumulation.

When intravenously administered to tumor-bearing nude mice, DPP-R quickly dispersed in blood capillary and then penetrated through the vascular endothelial cell (VEC) space to tumor tissue, relying on the typical enhanced permeability and retention (EPR) effect induced

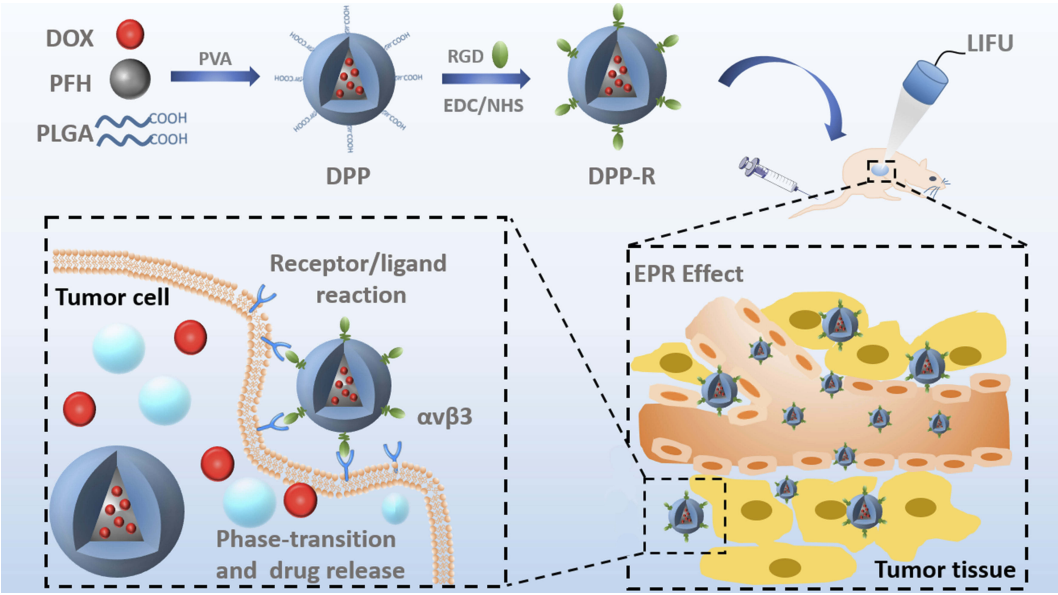

Figure 1 Schematic illustration of the assembly method, synthesizing process and theranostic procedures of the acoustic-responsive DPP-R, including double emulsion and carbodiimide method for synthesizing, active and passive targeting effect induced by receptor/ligand, and EPR effect and LIFU-mediated phase-transition and accurate drug release for theranostics.

by nanoscale particle size.[28,29] Besides the passive targeting, efficient active accumulation and intracellular uptake were generated via the combination of integrin $\alpha v\beta_3$, which is overexpressed on membranes of tumor cells and in neovascularization, with the specific ligand RGD peptide on DPP-R.[30] After certain amount of hours of reaction, LIFU was duly applied on tumor site to transiently expand VEC space and enhance membranes' permeability, which benefited the aggregation, phase-transition, and drug release of DPP-R for imaging and therapy.

To preliminarily evaluate the properties of DPP-R, various physicochemical detections were conducted. Firstly, DPP-R showed a uniform size and was homodisperse, as observed by optical microscope (Figure 2A). And TEM revealed its subtle core/shell spherical morphology (Figure 2B) with a certain average diameter at 367 nm (PDI=0.042) (Figure 2C). As DOX was encapsulated and RGD conjugated, the particle size appeared to be slightly increased (Figure2E), but did not alter the nanoscale characteristics of NPs. On the other hand, a distinct rise in negative electric potential was measured (Figure 2D) as the result of the connection with RGD, which facilitated mutual exclusion in blood and electrostatic adherence between DPP-R and cells during penetration and endocytosis.[31] The particle size and PDI value of DPP-R remained relatively constant in the three different media when stored at 4°C and measured at room temperature for 7 days (Figure 2F, Figure S1). Besides, no significant changes in its morphology features were observed according to SEM images (Figure S2), which strongly suggested the high stability of DPP-R and laid the foundation for further research.

The UV-Vis-NIR absorption curve of DPP showed a typical absorption peak as the curve of free DOX compared to the curve of PP (Figure 2G), which demonstrated DOX was successfully encapsulated by PLGA. Meanwhile, DOX presented a concentration-dependent rise in absorbance intensity from 3.75 μg/mL to 120 μg/mL at 483 nm (Figure 2H) and the concentration-absorbance intensity relationship was counted as a linear equation: $Y=0.018X+0.0552$ ($R^2=0.998$) (Figure 2I). Then the EE and LC were calculated as 41.2% and 2.58% respectively based on the equation.

To further examine drug-release profile, the experiment was carried out under different pH conditions. As shown in Figure 3, DOX released sequentially only less than 50% of the loading content within 72 h in both conditions without LIFU irradiation. Remarkably in this process, DOX was easier to release about 10% more content in acidic buffer, which indicated higher concentration and enhanced therapeutic efficiency in acidic tumor microenvironment.[32] However, the total effective drug remained insufficient on account of the condense polymer structure which meant that DOX could only escape from

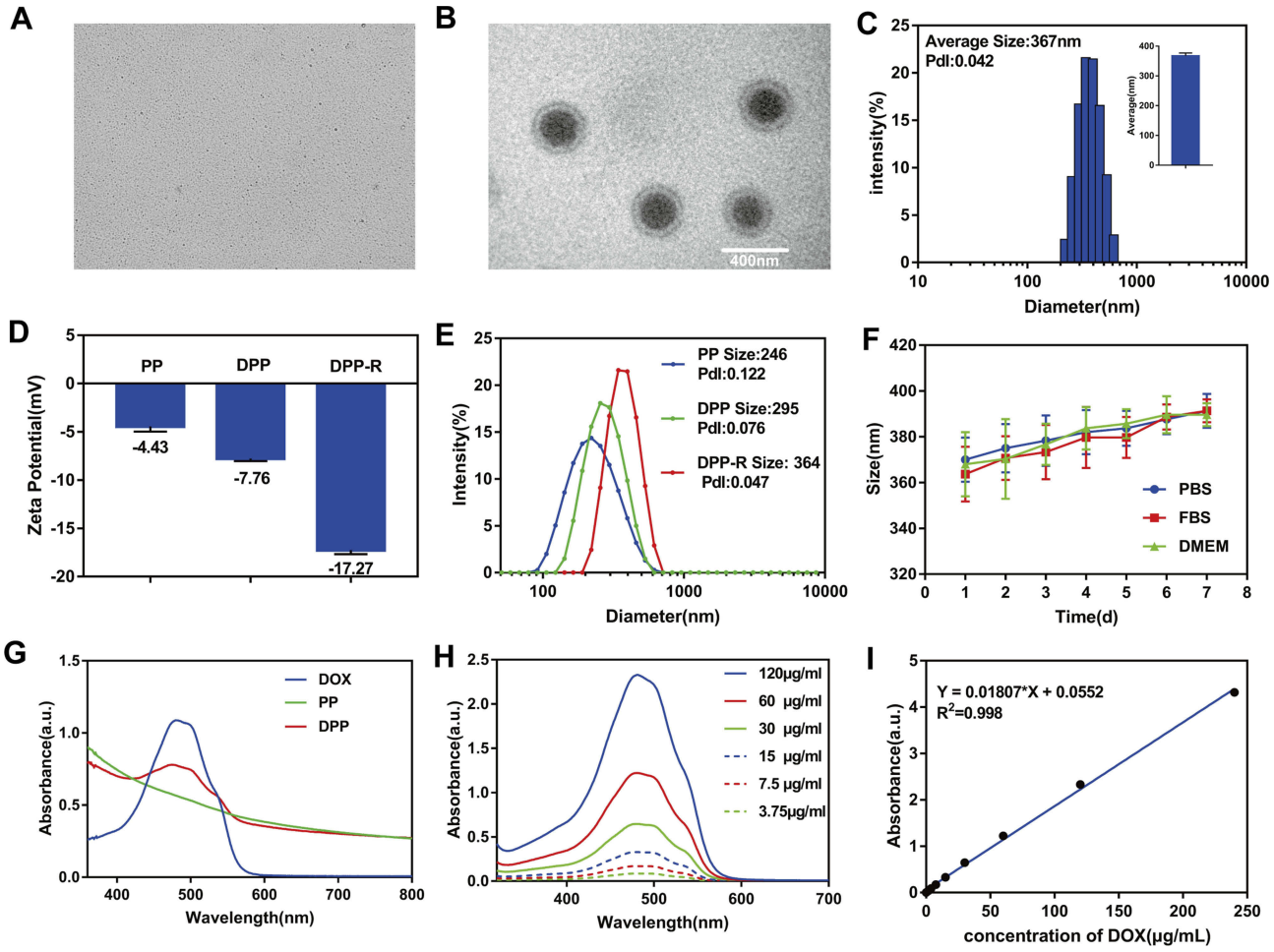

Figure 2 (**A**) Optical microscope image (×600). (**B**) TEM image. (**C**) Average size of DPP-R. (**D**) Zeta potential of PP, DPP, and DPP-R. (**E**) Size of PP, DPP, and DPP-R. (**F**) Size of DPP-R in PBS, FBS, and high glucose DMEM in 7 days. (**G**) The UV-Vis-NIR absorption curve of PP, DOX, and DPP. (**H**) The UV-Vis-NIR absorption curve of DOX in different concentrations. (**I**) Standard curve of DOX related to concentration and absorbance intensity. (The data were shown as mean±SD, n=3).

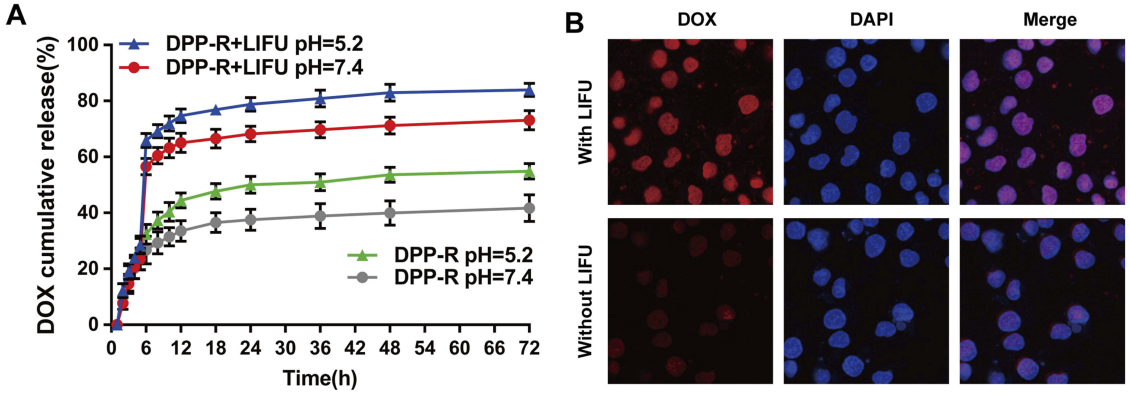

Figure 3 (**A**) Drug cumulative release of DPP-R in PBS (pH=5.2/7.4) at 37°C with or without LIFU irradiation at 6 h. (**B**) CLSM images of facilitated DOX release triggered by LIFU. The red fluorescence represented released DOX; the blue fluorescence marked cell nucleus (×400). (The data were shown as mean±SD, n=3).

the unsteady NPs with incomplete or irregular shell. On the contrary, after exposure to LIFU at 6 h, a burst release of about 30% increase in concentration was observed, and facilitated release also existed in acidic condition. Finally, about 80% of entrapped DOX released from NPs within 72 h. The instantaneous phase-transition triggered by LIFU blasted a big fraction of NPs inducing the burst release and left behind another fraction of transformational

MBs benefitting from the excellent elasticity of PLGA which allowed DOX to escape from the expanded porous shell steadily. This controlled DOX release behavior imparted an accurate anti-tumor ability to DPP-R which prospectively conquered the systemic toxicity to hematopoiesis, hepatic, nephric or cardiac function.

To verify the facilitated drug release and membranes' permeability induced by LIFU, two groups of MGC-803 cells were cultured with DPP for 24 h. After that, one group received LIFU while the other did not. As simply illustrated in Figure 3B, the red fluorescence of DOX in cell nucleus was evidently stronger in the group that received LIFU than the group that did not. The expectable phenomenon confirmed the cavitation effect of LIFU to control drug release and enhance penetration mentioned previously.

Bio-compatibility and bio-safety studies

Cytotoxicity, H&E staining, routine blood, and blood biochemistry were conducted to evaluate the bio-compatibility and bio-safety of the as-synthesized NPs in vitro and vivo which served as the important precondition for clinical translation. Satisfactory results were obtained: cell viability of the three groups (PP-R, PP, and LIFU) was all above 85% as assessed by CCK-8 assay (Figure 4A), indicating unubiquitous cytotoxicity of the materials (except chemotherapeutic DOX) used to synthesize NPs in vitro; the H&E staining of major organs of mice intravenously injected with PP-R for different periods showed no histological change compared with control group (Figure 4B), and all tested indicators of blood samples were within the normal range (Figure 4C), which sufficiently demonstrated that no acute or chronic physiological toxicity inherently existed in the fabricated NPs in

A

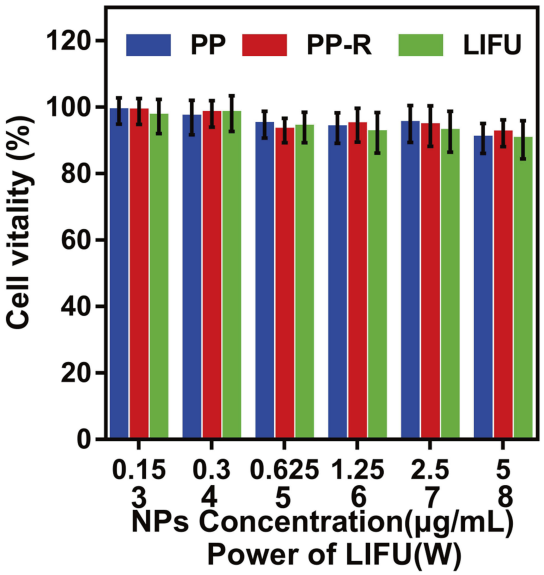

B

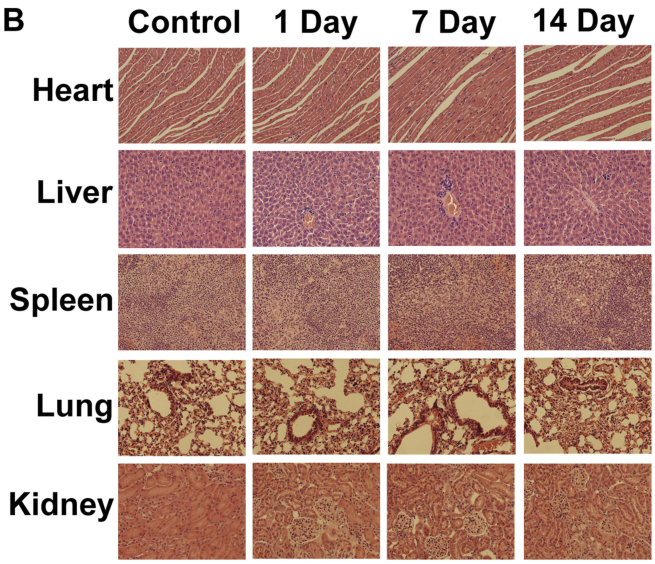

C

Group		RBC(10^9/L)	WBC(10^9/L)	HGB(g/L)	ALT(U/L)	ALP(U/L)	CREA(μmol/L)	BUN(mmol/L)
Saline	1 Day	9.23±0.56	5.33±1.61	169.43±8.58	72.56±16.34	147.47±23.53	10.56±1.35	6.27±1.05
	7 Day	8.96±1.07	4.78±0.66	157.72±11.36	78.47±13.73	136.75±34.67	10.28±0.62	5.96±0.68
	14 Day	9.94±0.63	5.84±0.49	164.85±6.62	74.68±10.51	143.52±17.94	9.94±0.72	6.44±1.12
PP	1 Day	9.71±0.85	5.26±1.12	155.83±8.58	75.95±11.67	159.35±14.74	10.75±1.55	5.73±0.39
	7 Day	8.92±0.72	4.53±0.75	162.84±11.36	73.83±8.64	138.69±26.58	11.21±1.03	6.57±0.73
	14 Day	9.76±0.46	4.37±1.04	159.54±8.45	75.68±6.38	142.85±19.64	10.73±1.29	6.36±1.24
PP-R	1 Day	9.32±1.01	5.15±0.88	164.29±8.67	78.45±9.37	136.84±21.63	9.77±0.42	5.81±0.63
	7 Day	9.08±0.55	5.83±1.01	157.39±12.63	71.4±8.63	140.67±24.81	11.06±1.44	6.62±0.52
	14 Day	10.11±0.37	5.17±0.94	158.85±9.47	77.58±5.95	133.74±24.84	10.93±0.79	6.79±0.68

Figure 4 Bio-compatibility and bio-safety of original materials. (**A**) Cell viability of MGC-803 after incubated with NPs for 24 h and tested by CCK-8 assay. (**B**) H&E staining of major organs of control group and PP-R group at 1 day, 7 days, and 14 days after being intravenously injected with PP-R (×400). (**C**) Major indicators of routine blood and blood biochemistry examination of control, PP, and PP-R groups at 1 day, 7 das, and 14 days. (The data were shown as mean±SD, n=3).

vivo. The high bio-compatibility and bio-safety guaranteed NPs'feasibility of further utility in the study.

Targeting ability and bio-distribution of DPP-R

According to reports, targeting ability effectively enhances specificity and therapy efficiency.[33,34] With the introduction of RGD, the anticipated targeting ability of DPP-R was assessed by CLSM. Firstly, as shown in Figure 5A, the red fluorescence of DOX and green fluorescence of RGD-FITC were almost overlapping, which indicated that NPs with DOX were connected with RGD-FITC successfully. The quantitative average binding efficiency of NPs and RGD-FITC was 85.77% as measured by FCM (Figure 5B). For investigating the cellular targeting ability of tumor cells over-expressing integrin $\alpha v\beta_3$, the red fluorescence representing NPs was significantly concentrated around the green membranes of MGC-803 cells labeled by DiO in targeting group which had been cultured with DPP-R for 3 hrs, while rare red fluorescence could be observed in non-targeting group co-incubated with DPP instead (Figure 5C). The quantitative average binding efficiency between NPs and cells of targeting group and non-targeting group was 80.32% and 3.42% respectively (Figure 5D), which strongly demonstrated the higher tumor-homing property of DPP-R compared to DPP, ascribed to the receptor/ligand effect.

FLI system was used to further evaluate the targeting ability and dynamic bio-distribution of NPs in tumor-bearing mice at predetermined times. Considering the fact that NPs would likely accumulate in liver tissue simultaneously due to the endocytosis of reticuloendothelial,[35] subcutaneous tumor models were chosen to be intravenously injected with targeting NPs (DPP-R) and non-targeting NPs (DPP) respectively. At 1 h post-injection, fluorescence was observed only around liver and spleen area in both groups, and then in the targeting group DPP-R gradually accumulated in the tumor tissue enough to reach a peak and be monitored by FLI at 6 h and still remained in the site at 24 h. Comparatively, no significant fluorescence was observed in the non-targeting group in tumor site during the 24 h (Figure 6A), illustrating an effective and time-dependent targeting ability of DPP-R. The fluorescence images and intensity of heart, liver, spleen, lung, kidney and tumor ex vivo were collected and quantified to further validate the accumulation of DPP-R in tumor site and the distribution in major organs after 24 h (Figure 6B). As expected, liver took in a big fraction of NPs in both groups for reticuloendothelial system with a little bit in spleen while no measurable fluorescence was distributed in other organs. The fluorescence intensity of excised tumor of targeting group remained 10-fold higher than that of non-targeting group (Figure 6C). Non-targeting NPs DPP were prevented from accumulating in tumor by high interstitial fluid pressure (IFP),[36] which was partially overcome by the reaction between receptor and ligand. The as-revealed pre-eminent active targeting ability and long circulation time of DPP-R gave it the potential to deliver anti-tumor agents and contrast agents accurately and efficiently for extravascular theranostics.

Ultrasound imaging generated from the phase-transition of DPP-R

PFH was an ideal phase change material (PCM) with a boiling point of 56°C offering subsequent gas for cavitation effect and US imaging.[37] It was considered safer than another common liquid fluorocarbon PFP, which was risky to apply in vivo for gas embolism generated by a lower boiling point of 29°C than body temperature.[38] To evaluate the proper power and duration of ADV effect of DPP-R, the NPs were exposed to LIFU with a power of 4 W, 6 W, and 8 W respectively and a duration 3–6 min. According to US images (Figure 7A), visualized microscopic images (Figure 7B), and average grayscale values in B-mode and CEUS mode (Figure 8B), the ADV effect exhibited a time/power-dependent trend which peaked at the parameter of 8 W for 5 min. When the parameter was lower than 8 W for 5 min, there were no or insufficient triggered MBs to optimize US images, while once the parameter exceeded 8 W for 5 min, most of the generated MBs collapsed and gradually disappeared for the higher unsteadiness than NPs. These results indicated that a certain stimulation was essential to arouse ADV effect of DPP-R and the vaporization of PFH was the precondition for CEUS; meanwhile, the destruction of excessive stimuli to NPs could not be ignored. Therefore, 8 W for 5 min was determined to be the preferable precondition.

To further explore the ADV potential of DPP-R for GC in vivo, LIFU irradiation and RGD conjugation was used as variable; therefore, three groups (DPP-R+LIFU, DPP-R, DPP+LIFU) of orthotopic tumor-bearing mice were observed with or without being exposed to LIFU after intravenous injection with different agents. In all groups no obvious CEUS signal before LIFU irradiation was obsersved. 6 hrs later, LIFU was applied to DPP-R

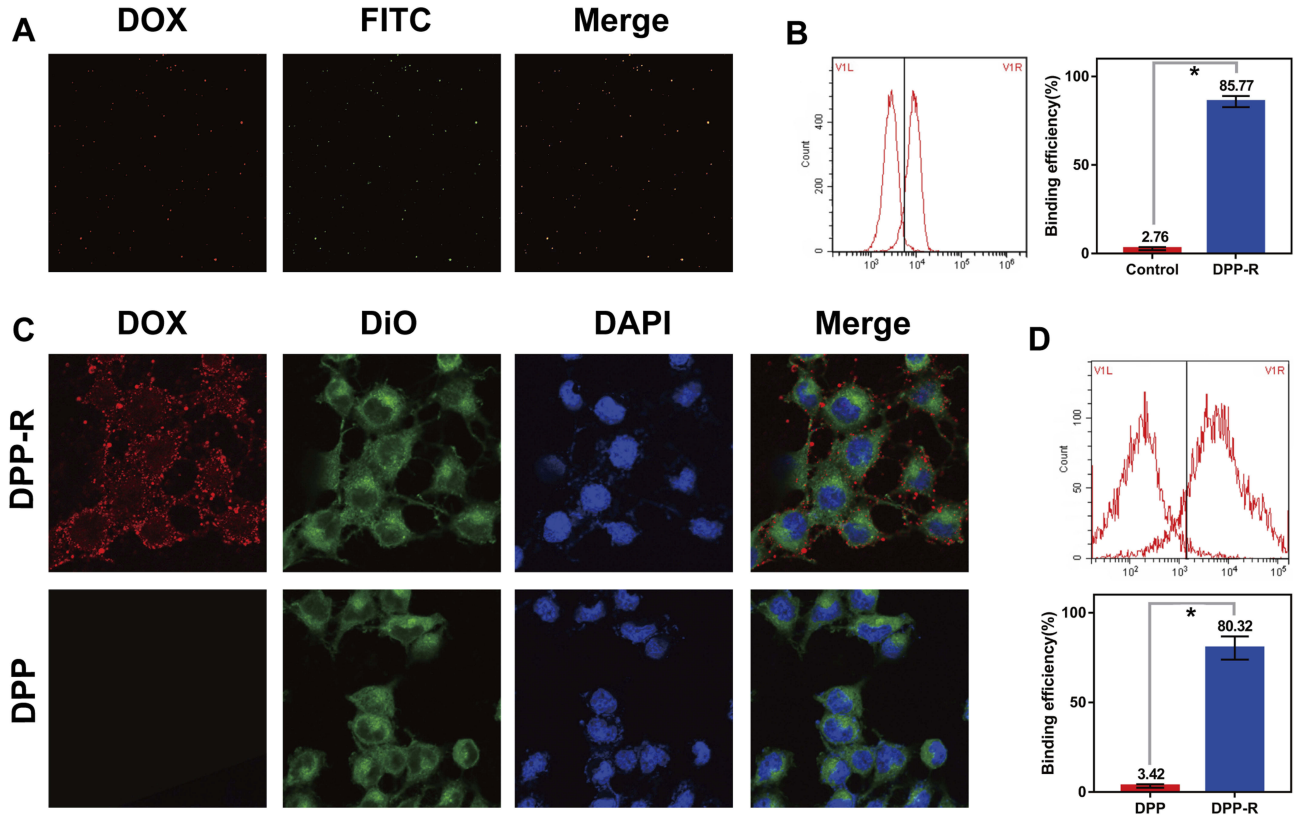

Figure 5 Targeting ability of DPP-R in vitro. (**A**) CLSM images of DPP-R. The red fluorescence represented encapsulated DOX; the green fluorescence represented RGD-FITC; the red and green fluorescence overlapped almost indicating that RGD successfully bound with DPP (×1000). (**B**) Binding efficiency between RGD and DPP measured by FCM. (**C**) CLSM images of MGC-803 incubated with DPP-R and DPP respectively for 3 h. The red fluorescence represented encapsulated DOX; the green fluorescence of DiO marked cell membranes and the blue fluorescence of DAPI marked cell nucleus (×400). (**D**) Binding efficiency between NPs and cells measured by FCM. (The data were shown as mean±SD, n=3, *p<0.05).

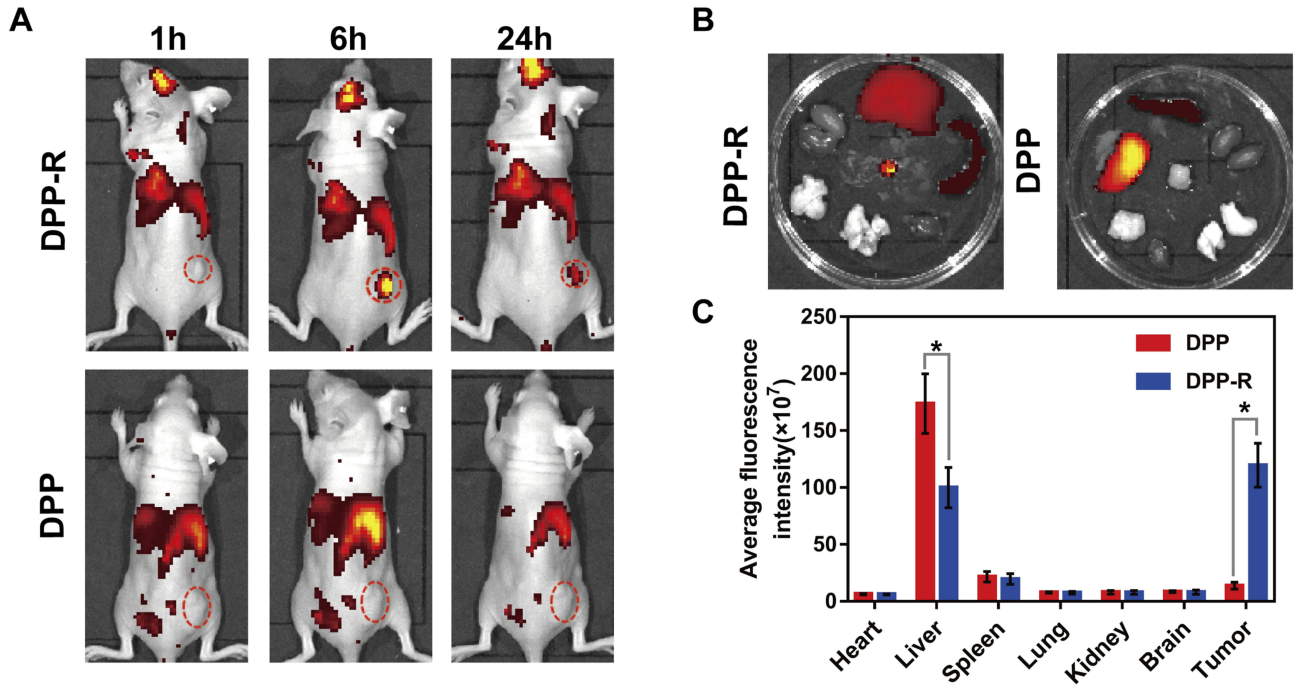

Figure 6 Targeting ability of DPP-R in vivo. (**A**) FLI images of nude mice after being intravenously injected with DPP-R and DPP respectively for 1 h, 6 h, and 24 h. (**B**) FLI images and the average fluorescence intensity (**C**) of major organs ex-vivo. (The data were shown as mean±SD, n=3, *p<0.05).

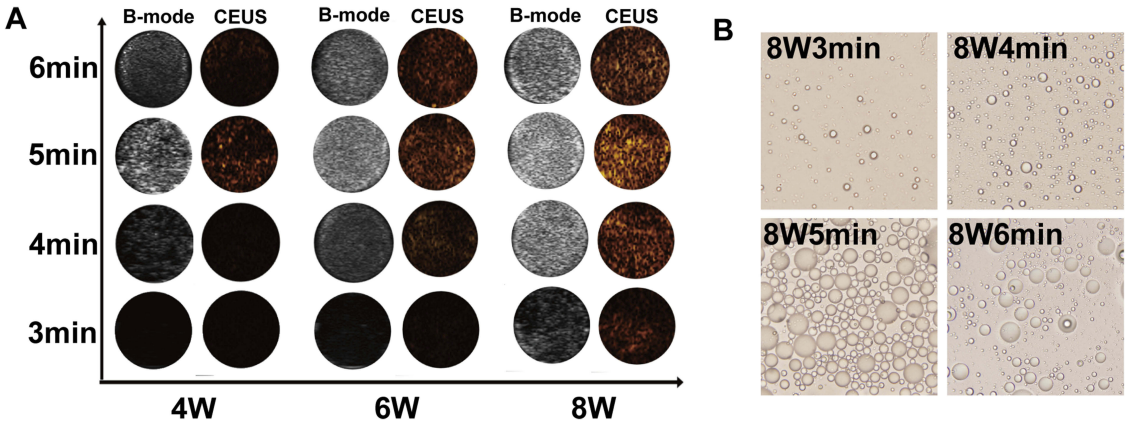

Figure 7 ADV imaging in vitro. (**A**) B-mode and CEUS images of DPP-R at different duration and power of LIFU. (**B**) Optical microscope images of phase-transition of DPP-R triggered by LIFU at a power of 8 W from 3 min to 6 min.

+LIFU group and DPP+LIFU group, the contrast-enhanced effect of DPP-R+LIFU group was significantly stronger than that of the other two groups (Figure 8A), which was consistent with the quantified grayscale values (Figure 8C). A noteworthy increase in grayscale value in B-mode and CEUS mode was detected in DPP-R+LIFU group with no remarkable change in DPP+LIFU or DPP-R groups. As revealed by the results, LIFU and RGD were both indispensable participators for targeting US imaging. Though the effective accumulation was facilitated by the receptor/ligand reaction absenting LIFU irradiation, DPP-R remained liquid core and hardly offered an US signal. Similarly, with the separate application of LIFU to enhance permeability and trigger liquid-to-gas transition at tumor lesion, insufficient NPs were actively aggregated intratumor for lacking of the RGD-mediated penetration and localization.

Precision chemotherapy

Besides improving US imaging ability of tumors, DOX was designed to be encapsulated in NPs aiming at giving it an anti-tumor ability. Preliminary toxicity assessment of DPP-R in vitro was surveyed by CCK-8 assay to provide the basis for the following application in vivo. The cell viability of all groups exhibited a concentration-dependent decreasing trend as the equal concentration of DOX increased (Figure 9A). Compared with free DOX, the cell viability of DPP-R+LIFU was always lower, which indicated that DPP-R combined with LIFU irradiation offered better anti-tumor efficiency. In addition, there was no severe cytotoxicity while incubated with DPP-R separately. This result was mainly related to the absence of LIFU which could induce drug release, NPs' penetration and cavitation effect.[39] Nevertheless, the cell viability of DPP+LIFU was higher than that of free DOX and DPP-R +LIFU because bare NPs could adhere to cells or be endocytosed without the participation of targeting ligand, which means DOX release was triggered extracellularly. On the other hand, it verified the importance and effectiveness of the specific binding between RGD and $\alpha v\beta_3$. Consequentially it was confirmed that DPP-R synergized with LIFU showed admirable potential in therapeutic efficiency.

Based on the considerable cytotoxicity to cells, further therapy in vivo was conducted with orthotopic tumor-bearing nude mice. Groups were divided as CCK-8 assay and saline was injected in control group (n=3 per group). 10 days after the tumors were transplanted, every mouse was intravenously injected with the respective agents. On account of the phase-transition and FLI results, the time point was determined at 6 h for the maximum accumulation of DPP-R to apply LIFU to tumor site. The same therapeutic strategy was carried out every 3 days for a total of 5 times. During the therapy, mice of the control group gained weight rapidly since the tumors received no therapeutic treatment (Figure 9B). On the contrary, the weight of mice in DOX group was observed to decline and two of them died after therapy, which clearly confirms the fatal toxicity and side effects of DOX.[40] Comparatively, the body weight of mice in DPP-R and DPP+LIFU groups increased slowly while a negligible change in weight was detected in DPP-R+LIFU group. After finishing the treatment, the orthotopic tumors were surgically exposed to be measured accurately (Figure 10A). The mean tumor weight of each group was as follows: control 1.75 g, free DOX group 0.85 g, DPP-R+LIFU

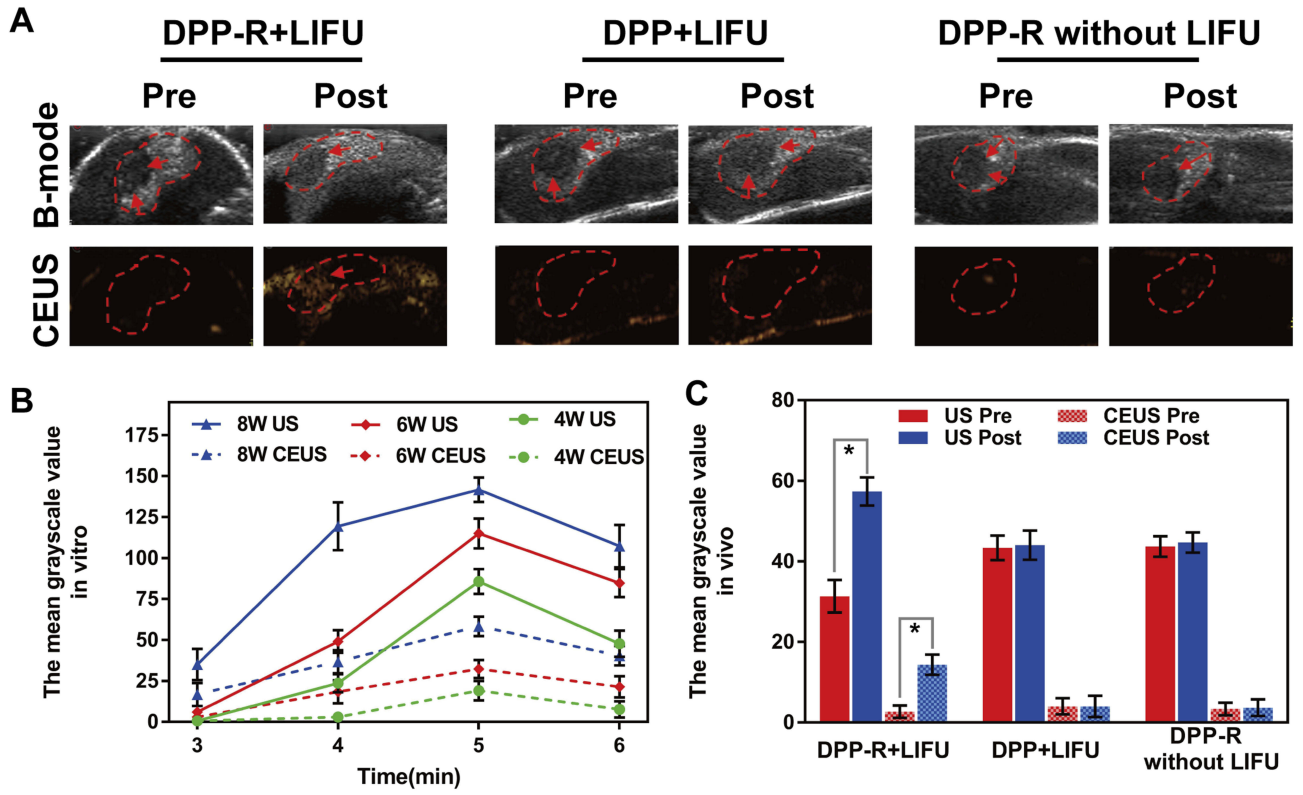

Figure 8 ADV imaging in vivo. (**A**) B-mode and CEUS images of orthotopic tumor-bearing mice at tumor site before and after LIFU irradiation. (**B**) The variation trend of the quantized mean grayscale values of B-mode and CEUS mode for different duration and power of LIFU in vitro. (**C**) The quantized mean grayscale values of B-mode and CEUS mode of tumor site (The data was exhibited as mean±SD, n=3, *p<0.05).

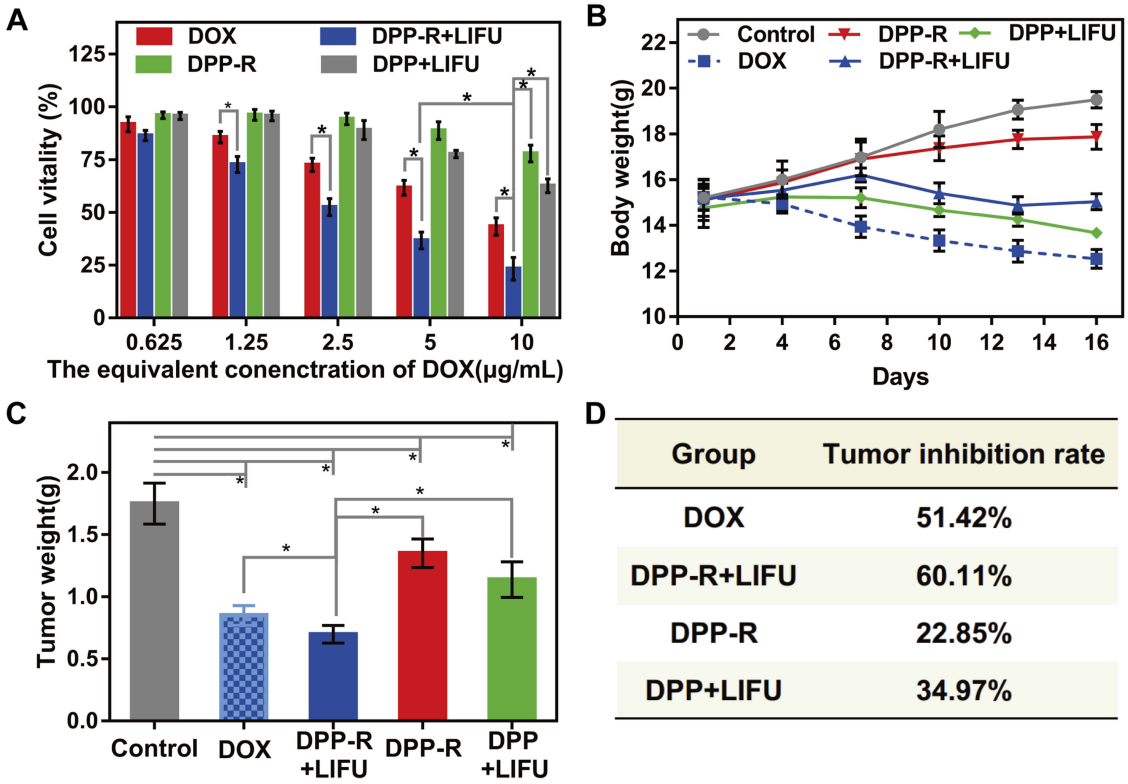

D

Group	Tumor inhibition rate
DOX	51.42%
DPP-R+LIFU	60.11%
DPP-R	22.85%
DPP+LIFU	34.97%

Figure 9 (**A**) Cell vitality of MGC-803 incubated with different formulations of different agents. (**B**) Body weight of orthotopic tumor-bearing nude mice in different groups during therapy period. (**C**) Posttreatment tumor weight and (**D**) tumor inhibition rate of orthotopic tumor-bearing nude mice in different groups. (The data were shown as mean±SD, n=3, *p<0.05).

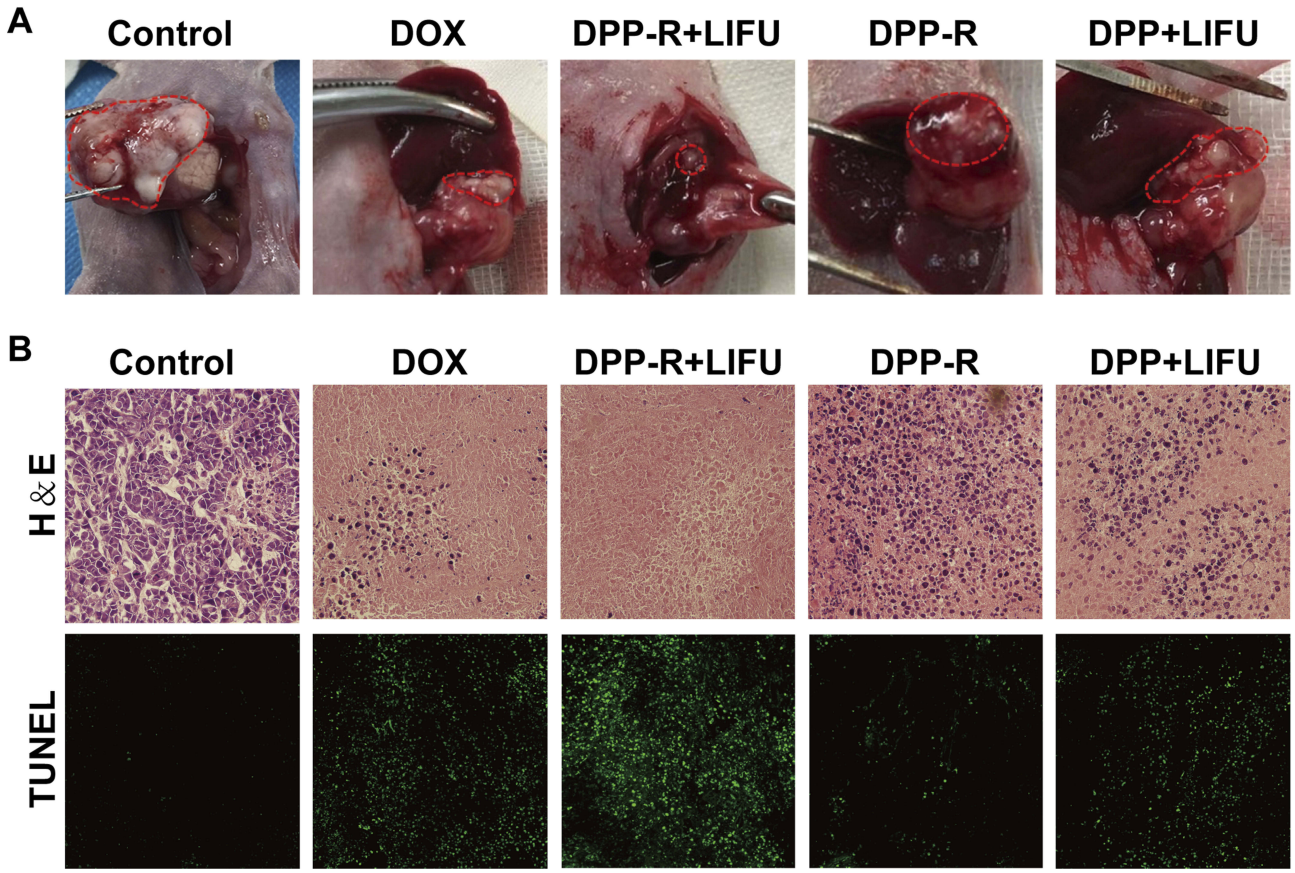

Figure 10 (**A**) Tumor images of orthotopic tumor-bearing nude mice in different groups after treatment. (**B**) H&E and TUNEL staining of tumors in different groups (×400).

group 0.70 g, DPP-R group 1.35 g, and DPP+LIFU group 1.14 g. As shown in Figure 9C, the tumor weight of free DOX group was significantly less than that of control group, while it was even more inhibited in DPP-R+LIFU group. The TIR of DPP-R+LIFU group reached 60.11%, nearly 10% more than free DOX group and over 2-fold more than the other groups (Figure 9D). The targeting aggregation response and acoustics-responsive drug-release ability endowed DPP-R with brilliant anti-tumor effect when combined with LIFU. The focused mechanical wave transitorily cavitated membranes, empowered vaporization, and promoted DOX release. Permeability was elevated with the tiny pores generated on membranes and burst release of DOX was intensified with the microjets induced by MBs' destruction,[31] which therefore enhanced the therapy efficiency and overcame the side effects. When rejecting the targeting ligand or the drug trigger, as conducted in DPP-R and DPP+LIFU group, the capability to combat tumor weakened dramatically. All the evidence implied the therapeutic effect and bio-safety of DPP-R NPs combined with LIFU, which effectively inhibited the tumor growth and ameliorated the systemic adverse effects of DOX administration.

The histopathology of tumors was used to analyze the apoptosis in different groups post-treatment, including H&E and TUNEL staining. As shown in Figure 10B, masses of nucleus were destroyed in DPP-R+LIFU group and DOX group compared with control group, while plenty of normal cells still survived in DPP-R and DPP+LIFU groups as shown by H&E staining. In addition, the green fluorescence of DPP-R+LIFU group was the strongest, which represented the apoptotic cell in TUNEL staining. The same trend was observed in histopathology as in vivo therapy further illustrated the anti-tumor effect of DPP-R NPs.

In view of the fatal adverse effects of DOX, major organs in different groups were sectioned for histopathology analysis with H&E staining and routine blood and biochemistry were examined for bio-functional assessment. Myocardial interstitial vacuolar degeneration, hepatocyte swelling, mussily arranged hepatic cord, and glomeruli atrophy were observed in DOX group and DPP+LIFU group (Figure 11A), indicating histological damage of organs. And blood indicators representing hematopoietic, cardiac, hepatic, and nephric function

A

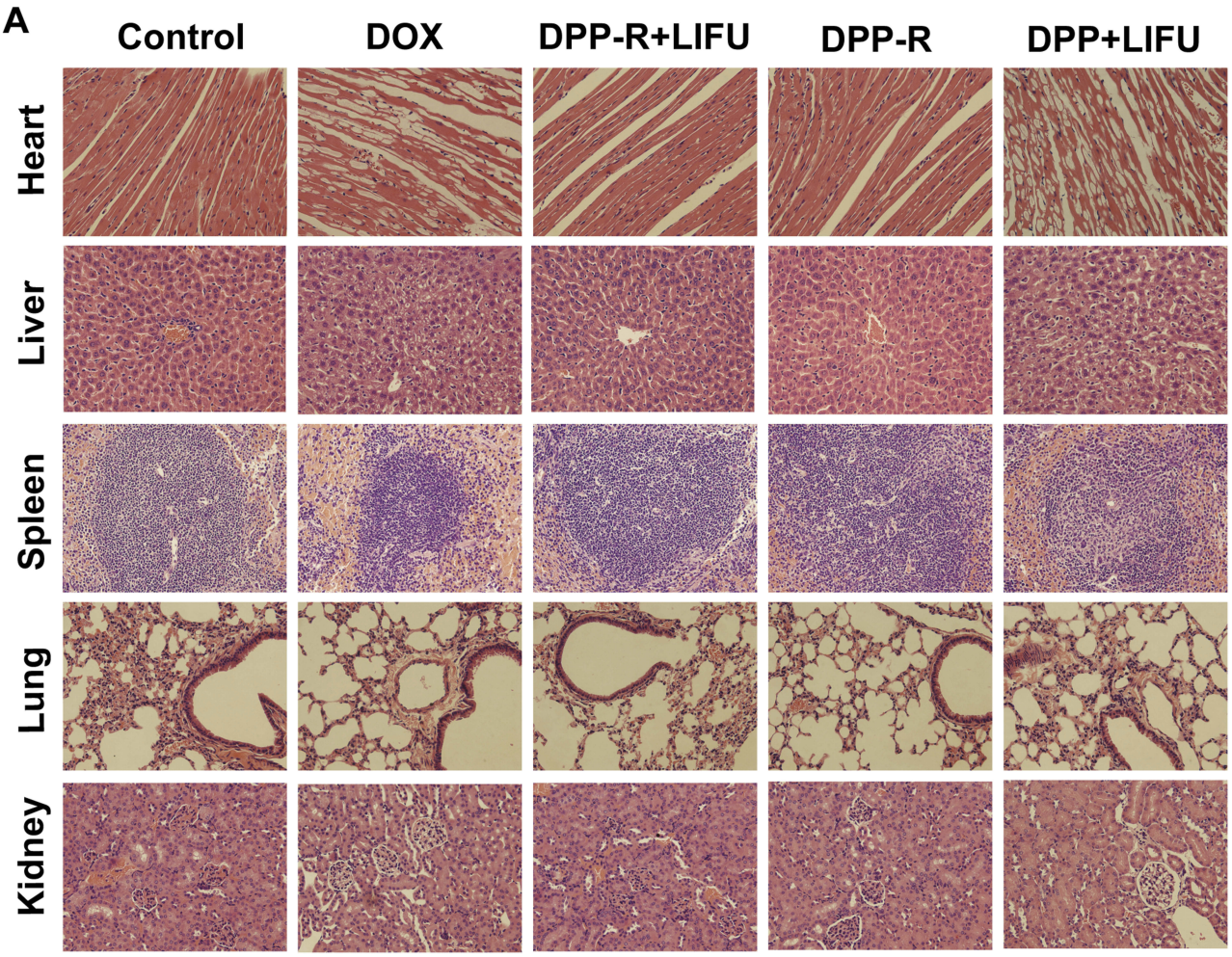

B

Group	WBC(10^9/L)	PLT(10^9/L)	LDH/α-HBDH	AST/ALT	TBIL(μmol/L)	CREA(μmol/L)	BUN(mmol/L)
Control	5. 38±0. 97	958. 73±85. 63	3. 07±0. 32	2. 41±0. 57	1. 42±0. 35	10. 57±1. 27	6. 34±0. 76
DOX	2. 57±0. 42*	623. 72±95. 26*	2. 14±0. 26*	4. 29±1. 03*	2. 74±0. 63*	17. 43±2. 54*	12. 47±2. 05*
DPP-R+LIFU	4. 92±0. 56	886. 36±48. 42	3. 11±0. 22	2. 73±0. 48	1. 37±0. 28	10. 93±0. 84	5. 93±0. 59
DPP-R	3. 56±0. 37*	802. 46±54. 58*	2. 85±0. 35	2. 84±0. 61	1. 44±0. 24	13. 75±0. 72*	8. 10±0. 66*
DPP+LIFU	2. 72±0. 51*	676. 63±76. 26*	2. 36±0. 18*	3. 79±0. 72*	2. 63±0. 49*	9. 94±1. 75	11. 94±1. 75*

Figure 11 (**A**) H&E staining of major organs of nude mice in different groups after therapy. Myocardial interstitium existed vacuolar degeneration, hepatocyte swelled, hepatic cord arranged mussily and glomeruli atrophied in DOX and DPP+LIFU groups. (**B**) Blood indicators of different groups including hematopoietic, cardiac, hepatic and nephric function. (The data were shown as mean±SD, n=3, *p<0.05).

such as WBC, PLT, LDH/α-HBDH, AST/ALT, TBIL, CREA, and BUN had significant anomalies in DOX group and DPP+LIFU group, demonstrating bio-functional disorders induced by DOX (Figure 11B). Fortunately, all the histological and blood biochemical results exhibited a healthy tissue structure and function in DPP-R+LIFU group, which convincingly shows a great reversal of adverse effects of DOX attributed to the encapsulation by PLGA, localized accumulation by receptor/ligand reaction, and accurate drug release triggered by LIFU.

Conclusion

In this study, the multifunctional DPP-R was successfully synthesized by assembling PFH, DOX, and RGD into a polymer matrix and was endowed with contrast-enhanced imaging ability and precise targeting nano-chemotherapy

for combating GC. We had mainly verified the active targeting ability and acoustic-responsive phase-transition triggered by LIFU for US imaging. In addition, we had sequentially confirmed the localized drug accumulation controlled by LIFU for light-side-effect therapy. In summary, with the synergy of LIFU, the elaborately fabricated DPP-R possessed the advantageous capability of: 1) non-invasive extraordinary targeting and accurate drug release ability through intravenous administration; 2) facilitated penetration, sustained accumulation, enhanced anti-tumor effect, decreased adverse effects, and prolonged circulation; 3) high bio-safety and bio-compatibility for clinical translation.

Acknowledgment

The authors greatly acknowledge the financial support from the National Nature Science Foundation of China (grant no. 31630026, 81630047), Chongqing Foundation and Cutting-edge Research Projects (csct2016jcyjA0161) and the technical assistance from Chongqing Key Laboratory of Ultrasound Molecular.

Disclosure

The authors report no conflicts of interest in this work.

References

1. Ferlay J, Soerjomataram I, Dikshit R, et al. Cancer incidence and mortality worldwide: sources, methods and major patterns in GLOBOCAN 2012. *Int J Cancer*. 2015;136:E359–E386. doi:10.1002/ijc.29210
2. Taieb J, Moehler M, Boku N, et al. Evolution of checkpoint inhibitors for the treatment of metastatic gastric cancers: current status and future perspectives. *Cancer Treat Rev*. 2018;66:104–113. doi:10.1016/j.ctrv.2018.04.004
3. Wang J, Aryal M, Zhong Q, Vyas D, Airan R. Noninvasive ultrasonic drug uncaging maps whole-brain functional networks. *Neuron*. 2018;100:728–738.e727. doi:10.1016/j.neuron.2018.10.042
4. Yildirim A, Shi D, Roy S, et al. Nanoparticle-mediated acoustic cavitation enables high intensity focused ultrasound ablation without tissue heating. *ACS Appl Mater Interfaces*. 2018;10:36786–36795. doi:10.1021/acsami.8b15368
5. Tang H, Guo Y, Peng L, et al. In Vivo targeted, responsive, and synergistic cancer nanotheranostics by magnetic resonance imaging-guided synergistic high-intensity focused ultrasound ablation and chemotherapy. *ACS Appl Mater Interfaces*. 2018;10:15428–15441. doi:10.1021/acsami.8b01967
6. Alexander H, Geoffrey L, Katheryne W, Kimberly H, Stanislav E. Indocyanine green-loaded photoacoustic nanodroplets: dual contrast nanoconstructs for enhanced photoacoustic and ultrasound imaging. *ACS Nano*. 2014;8:250–259. doi:10.1021/nn403527r
7. Luke GP, Hannah AS, Emelianov SY. Super-resolution ultrasound imaging in vivo with transient laser-activated nanodroplets. *Nano Lett*. 2016;16:2556. doi:10.1021/acs.nanolett.6b00108
8. Dallapiazza RF, Timbie KF, Holmberg S, et al. Noninvasive neuromodulation and thalamic mapping with low-intensity focused ultrasound. *J Neurosurg*. 2018;128:875–884. doi:10.3171/2016.11.JNS16976
9. Li L, Yang S, Song L, et al. An endogenous vaccine based on fluorophores and multivalent immunoadjuvants regulates tumor micro-environment for synergistic photothermal and immunotherapy. *Theranostics*. 2018;8:860–873. doi:10.7150/thno.19826
10. Meng Y, Suppiah S, Surendrakumar S, Bigioni L, Lipsman N. Low-intensity MR-guided focused ultrasound mediated disruption of the blood-brain barrier for intracranial metastatic diseases. *Front Oncol*. 2018;8:338. doi:10.3389/fonc.2018.00338
11. Wang X, Yan F, Liu X, et al. Enhanced drug delivery using sonoactivatable liposomes with membrane-embedded porphyrins. *J Control Release*. 2018;286:358–368. doi:10.1016/j.jconrel.2018.07.048
12. Chereddy K, Payen V, Préat V. PLGA: from a classic drug carrier to a novel therapeutic activity contributor. *J Control Release*. 2018;289:10–13. doi:10.1016/j.jconrel.2018.09.017
13. Gu B, Sun X, Papadimitrakopoulos F, Burgess DJ. Seeing is believing, PLGA microsphere degradation revealed in PLGA microsphere/PVA hydrogel composites. *J Control Release*. 2016;228:170–178. doi:10.1016/j.jconrel.2016.03.011
14. Mylonaki I, Allémann E, Delie F, Jordan O. Imaging the porous structure in the core of degrading PLGA microparticles: the effect of molecular weight. *J Control Release*. 2018;286:231–239. doi:10.1016/j.jconrel.2018.07.044
15. Zhao H, Wu M, Zhu L. Cell-penetrating peptide-modified targeted drug-loaded phase-transformation lipid nanoparticles combined with low-intensity focused ultrasound for precision theranostics against hepatocellular carcinoma. *Theranostics*. 2018;8:1892–1910. doi:10.7150/thno.22386
16. Zhu L, Zhao H, Zhou Z, et al. Peptide-functionalized phase-transformation nanoparticles for low intensity focused ultrasound-assisted tumor imaging and therapy. *Nano Lett*. 2018;18:1831–1841. doi:10.1021/acs.nanolett.7b05087
17. Xi J, Li M, Jing B, et al. Long-Circulating Amphiphilic Doxorubicin for Tumor Mitochondria-Specific Targeting. *ACS Appl Mater Interfaces*. 2018;10:43482–43492. doi:10.1021/acsami.8b17399
18. Marques-Aleixo I, Santos-Alves E, Oliveira P, Moreira P, Magalhães J, Ascensão A. The beneficial role of exercise in mitigating doxorubicin-induced Mitochondrionopathy. *Biochim Biophys Acta Rev Cancer*. 2018;1869:189–199. doi:10.1016/j.bbcan.2018.01.002
19. Liu J, Shang T, Wang F, et al. Low-intensity focused ultrasound (LIFU)-induced acoustic droplet vaporization in phase-transition perfluoropentane nanodroplets modified by folate for ultrasound molecular imaging. *Int J Nanomedicine*. 2017;12:911–923. doi:10.2147/IJN.S122667
20. Chan L, Gao P, Zhou W, et al. Sequentially Triggered Delivery System of Black Phosphorus Quantum Dots with Surface Charge-Switching Ability for Precise Tumor Radiosensitization. *ACS Nano*. 2018;12:12401–12415. doi:10.1021/acsnano.8b06483
21. Mao B, Liu C, Zheng W, et al. Cyclic cRGDfk peptide and Chlorin e6 functionalized silk fibroin nanoparticles for targeted drug delivery and photodynamic therapy. *Biomaterials*. 2018;161:306–320. doi:10.1016/j.biomaterials.2018.01.045
22. Zhang L, Wang D, Yang K, et al. Mitochondria-Targeted Artificial "Nano-RBCs" for Amplified Synergistic Cancer Phototherapy by a Single NIR Irradiation. *Adv Sci*. 2018;5:1800049. doi:10.1002/advs.201800049
23. Tang J, Zhang R, Guo M, et al. Nucleosome-inspired nanocarrier obtains encapsulation efficiency enhancement and side effects reduction in chemotherapy by using fullerenol assembled with doxorubicin. *Biomaterials*. 2018;167:205–215. doi:10.1016/j.biomaterials.2018.03.015
24. Zhang M, Hagan CTT, Min Y, et al. Nanoparticle co-delivery of wortmannin and cisplatin synergistically enhances chemoradiotherapy and reverses platinum resistance in ovarian cancer models. *Biomaterials*. 2018;169:1–10. doi:10.1016/j.biomaterials.2018.03.055
25. You Y, Wang Z, Ran H, et al. Nanoparticle-enhanced synergistic HIFU ablation and transarterial chemoembolization for efficient cancer therapy. *Nanoscale*. 2016;8:4324–4339. doi:10.1039/c5nr08292g

26. Guo Y, Wang X, Chen Y, et al. A light-controllable specific drug delivery nanoplatform for targeted bimodal imaging-guided photothermal/chemo synergistic cancer therapy. *Acta Biomater*. 2018;80:308–326. doi:10.1016/j.actbio.2018.09.024
27. Peng Y, Li Q, Seekell R, et al. Tunable Nonlinear Acoustic Reporters Using Micro- and Nanosized Air Bubbles with Porous Polymeric Hard Shells. *ACS Appl Mater Interfaces*. 2019;11–12. doi:10.1021/acsami.8b16737
28. Hu Z, Li X, Yuan M, et al. Study on the effectiveness of ligand reversible shielding strategy in targeted delivery and tumor therapy. *Acta Biomater*. 2019;83:349–358. doi:10.1016/j.actbio.2018.11.021
29. Wang HF, Ran R, Liu Y, et al. Tumor-Vasculature-on-a-Chip for investigating nanoparticle extravasation and tumor accumulation. *ACS Nano*. 2018;12:11600–11609. doi:10.1021/acsnano.8b06846
30. Xiao Y, Zhang Q, Wang Y, et al. Dual-functional protein for one-step production of a soluble and targeted fluorescent dye. *Theranostics*. 2018;8:3111–3125. doi:10.7150/thno.24613
31. Cao Y, Chen Y, Yu T, et al. Drug release from phase-changeable nanodroplets triggered by low-intensity focused ultrasound. *Theranostics*. 2018;8:1327–1339. doi:10.7150/thno.21492
32. Zhang P, Wang J, Chen H, et al. Tumor microenvironment-responsive ultrasmall nanodrug generators with enhanced tumor delivery and penetration. *J Am Chem Soc*. 2018;140:14980–14989. doi:10.1021/jacs.8b09396
33. Gopinath P, Mahammed A, Ohayon S, Gross Z, Brik A. Understanding and predicting the potency of ROS-based enzyme inhibitors, exemplified by naphthoquinones and ubiquitin specific protease-2. *Chem Sci*. 2016;7:7079–7086. doi:10.1039/c6sc02758j
34. Sithamparanathan S, Nair A, Thirugnanasothy L, et al. Survival in portopulmonary hypertension: outcomes of the United Kingdom National Pulmonary Arterial Hypertension Registry. *J Heart Lung Transplant*. 2017;36:770–779. doi:10.1016/j.healun.2016.12.014
35. Shao D, Lu MM, Zhao YW, et al. The shape effect of magnetic mesoporous silica nanoparticles on endocytosis, biocompatibility and biodistribution. *Acta Biomater*. 2017;49:531–540. doi:10.1016/j.actbio.2016.11.007
36. Chen B, Dai W, Mei D, et al. Comprehensively priming the tumor microenvironment by cancer-associated fibroblast-targeted liposomes for combined therapy with cancer cell-targeted chemotherapeutic drug delivery system. *J Control Release*. 2016;241:68–80. doi:10.1016/j.jconrel.2016.09.014
37. Zhao Y, Song W, Wang D, et al. Phase-Shifted PFH@PLGA/Fe3O4 nanocapsules for MRI/US Imaging and photothermal therapy with near-infrared irradiation. *ACS Appl Mater Interfaces*. 2015;7:14231–14242. doi:10.1021/acsami.5b01873
38. Aydin O, Vlaisavljevich E, Yuksel Durmaz Y, Xu Z, ElSayed ME. Noninvasive ablation of prostate cancer spheroids using acoustically-activated nanodroplets. *Mol Pharm*. 2016;13:4054–4065. doi:10.1021/acs.molpharmaceut.6b00617
39. Wang J, Jiao Y, Shao Y. The effect of plasma pretreatment and cross-linking degree on the physical and antimicrobial properties of Nisin-Coated PVA Films. *Materials (Basel, Switzerland)*. 2018;11. doi:10.3390/ma11081451
40. Johnson R, Shabalala S, Louw J, et al. Aspalathin Reverts Doxorubicin-Induced Cardiotoxicity through Increased Autophagy and Decreased Expression of p53/mTOR/p62 Signaling. Molecules. 2017;22:1589. doi:10.3390/molecules22101589